



In-plane carrier regulation and hydrogen adsorption/desorption optimization of P₄ molecule anchored Vs-ZnIn₂S_{4-x} for improve photocatalytic activity

Qingjie Luan^a, Xiangdong Xue^a, Hongtai Feng^a, Lu Tao^{a,*}, Dongxue Zhou^a, Tengfei Chen^a, Mengxi Tan^b, Wenjun Dong^{a,c,**}

^a Beijing Advanced Innovation Center for Materials Genome Engineering, Beijing Key Laboratory of Function Materials for Molecule & Structure Construction, School of Materials Science and Engineering, University of Science and Technology Beijing, Beijing 100083, PR China

^b Beijing Advanced Innovation Center for Materials Genome Engineering Institute for Advanced Materials and Technology University of Science and Technology Beijing, Beijing 100083, PR China

^c Shunde Graduate School of University of Science and Technology Beijing, Foshan 528399, PR China



ARTICLE INFO

Keywords:

Molecular-type cocatalysts
Anchored
Electron-rich
Adsorption/desorption barrier
Photocatalyst

ABSTRACT

Molecular-type cocatalysts can achieve the maximum electron transfer and minimum light absorption loss by virtue of their size advantage. Herein, a novel hydrophilic molecule-semiconductor hybrid P₄@Vs-ZnIn₂S_{4-x} photocatalyst was successfully developed by in-situ P₄ molecular anchoring on S defect ZnIn₂S_{4-x} (Vs-ZnIn₂S_{4-x}). The electron-rich P₄ molecules are anchored on the Zn-S₄ surface through S vacancies, forming Zn-P and S-P bonds that can promote electron injection from the electron-rich P₄ molecular to Vs-ZnIn₂S_{4-x} substrate and reduce the adsorption/desorption barrier of H intermediate on S atom of Zn-S₄ plane. Meanwhile, the electrostatic potential depression around P₄ promoted the directional migration of in-plane photogenerated electrons, and pooled electrons to the highly active P sites and S sites, thereby accelerating the kinetics of hydrogen evolution. As a result, P₄@Vs-ZnIn₂S_{4-x} achieves an optimal photocatalytic hydrogen evolution activity of 26.1 mmol g⁻¹ h⁻¹ under visible light, which is 6.2 times higher than 4.2 mmol g⁻¹ h⁻¹ for Vs-ZnIn₂S_{4-x}.

1. Introduction

Photocatalytic hydrogen production is considered as an appealing technology to solve sustainable energy and environmental issues [1–6]. To date, various semiconductor photocatalysts, such as TiO₂ [7,8], C₃N₄ [9,10], and ZnIn₂S₄ [11–13], have been developed for the solar-to-hydrogen conversion [14–16]. Especially, ultrathin ZnIn₂S₄ nanosheets with suitable band structure corresponding to visible-light response, unique tunable electronic structure and high specific surface area, is an excellent candidate for photocatalytic hydrogen evolution [17–22]. However, the excessive electronegativity of S atoms on the base plane of ZnIn₂S₄, with a strong interaction between hydrogen and sulfur ($\Delta G_{H^*} = -1.58$ eV), suppress the desorption of H atoms and result in a high kinetic barrier of hydrogen evolution [23–26].

Up to date, atomic doping or heterostructure constructing has been successfully developed to tune the adsorption free energy of H atom (G_{H^*}) [27–29]. Atomic doping (Ni, Cu, etc.) can increase the electron density near the S atoms by biasing the electron pair toward S atoms in the metal-sulfur (M-S) bond, which effectively reduces hydrogen adsorption on S atom of ZnIn₂S₄ surface [30,31]. While the uncontrolled atomic dopant only realizes a trace amount of doping. Besides, the doping centers usually trap photogenerated electrons and inhibit electron transportation to the activated S atom, thus resulting that the S atom active center losing the catalytic function [32,33]. For heterojunction constructing, the Fermi level difference drive the electrons toward ZnIn₂S₄ and increase electron density around the S atom [6,28,34]. However, only the edge S site actually work due to the most activated S sites in the interfacial region are blocked by second phase [35,36].

* Corresponding author.

** Corresponding author at: Beijing Advanced Innovation Center for Materials Genome Engineering, Beijing Key Laboratory of Function Materials for Molecule & Structure Construction, School of Materials Science and Engineering, University of Science and Technology Beijing, Beijing 100083, PR China.

E-mail addresses: xiaolu_tao@sina.com (L. Tao), wdong@ustb.edu.cn (W. Dong).

With its unique size, the molecular co-catalyst has high atomic utilization, while the entire P_4 molecular located in the built-in electric field, allows electrons well transferred throughout the P_4 to promote the reaction. Furthermore, the molecular scale size also minimizes the shielding effect of light and active sites, ensuring sufficient light absorption and active site exposure of the host catalyst. With the aim of enhancing the photocatalytic performance of $ZnIn_2S_4$, molecular co-catalysts are also desired to possessing the following functions: a) effectively inject electron to $ZnIn_2S_4$ to improve the adsorption and desorption of S sites; and b) ensuring the activated S atoms effectively capture photogenerated electrons. Based on this, a novel molecular co-catalyst modified $Vs\text{-}ZnIn_2S_{4-x}$ ($P_4\text{@}Vs\text{-}ZnIn_2S_{4-x}$) was synthesized, in which the P_4 molecular anchored on the S defects of half-unit-cell $ZnIn_2S_4$. The P_4 molecules are stabilized on the $Vs\text{-}ZnIn_2S_{4-x}$ surface through stable chemical bonding (P-Zn and P-S bonds). Moreover, the P_4 molecules inject electrons into $Vs\text{-}ZnIn_2S_{4-x}$ through interface P-Zn and P-S bridges, thus weakening the S-H bond strength and then conducting to H desorption [37–39]. In addition, the built-in electric field between P_4 and $Vs\text{-}ZnIn_2S_{4-x}$ boosts directional migration of electron from P_4 molecular to $Vs\text{-}ZnIn_2S_{4-x}$, resulting in the electrostatic potential depression, which drives the in-plane electrons into the highly active region and activates the catalytic activity of entire basal plane. The P_4 molecule co-catalyst, bridging the gap between single atom and heterojunction semiconductor photocatalyst, opens up a new avenue for catalysts designing in the molecular scale.

2. Experimental

2.1. Characterization

The crystalline structure and phase were characterized by powder X-ray diffraction (XRD, Bruker D8-Advance) with Cu K α radiation (40 kV, 40 Ma, $\lambda = 1.5406 \text{ \AA}$). The XRD pattern was record from 10° to 80° (20) with a scanning step of 5 min $^{-1}$. The morphologies and microscope were characterized by scanning electron microscope (SEM, Hitachi SU 8010). The high-resolution transmission electron microscope and elemental mapping were recorded with a JEOL 2200FS. The HAADF-STEM images were obtained from a JEOL JEM-ARM200F TEM/STEM with a spherical aberration corrector. Determination of the elements content has been determined taken by means of inductively coupled plasma optical emission spectrometer (Agilent, ICP-OES 730). X-ray photoelectron spectroscopy (XPS) data were recorded via an ESCALAB 250 Xi system (Thermo Electron Corporation). Room-temperature electron paramagnetic resonance (EPR) spectra was measured by EPR spectrometer (Bruker, A300–10/12). The FluorMAX-4 spectrophotometer was applied to get photoluminescence (PL) spectra. The time-resolved photoluminescence spectroscopy was characterized by an FLS 980 fluorescence spectrometer with excitation at 475 nm. Photocurrent measurements was carried out in a three-electrode cell system by applying CHI660E electrochemical station under a 300 W Xe arc lamp as a light source. UV-vis diffuse reflectance spectra (UV-vis DRS) were recorded at the range from 300 to 800 nm by a Shimadzu UV-2550, and $BaSO_4$ was applied as a reflectance standard. Electrochemical impedance spectroscopy (EIS) and Mott-Schottky plots was performed on a CHI660D with a three-electrode cell at room temperature. Electrochemical measurements were carried out in Na_2SO_4 (0.5 M, PH=6.8) solution, and a graphite sheet as the counter electrode, standard calomel electrode (SCE) as the reference electrode, and the catalysts on the fluoride tin oxide (FTO) as the working electrode. X-ray absorption fine structure (XAFS) spectra at S K-edge and P K-edge were performed at 4B7A beamline of Beijing Synchrotron Radiation Facility (BSRF), China. 4B7A beamline is equipped with a Si (111) double crystal monochromator which was detuned to eliminate higher harmonics. XAFS spectra at Zn K-edge were performed at 4B9A beamline of Beijing Synchrotron Radiation Facility (BSRF), China. XAFS measurements at In K-edge were conducted at the beamline (BL14W1) of Shanghai National

Synchrotron Radiation Facility (SSRF, China). The EXAFS data were disposed according to the standard procedures through the ATHENA module implemented in the IFEFFIT software packages. The k^3 -weighted $\chi(k)$ data in the k-space ranging from 3 to 13.5 \AA^{-1} were Fourier transformed to real (R) space using a hanging window ($dk=1.0 \text{ \AA}^{-1}$) to separate the EXAFS contributions from different coordination shells. To obtain the detailed structural parameters around the In centers in the as-prepared samples, the quantitative curve-fittings were carried out for the Fourier transformed $k^3 \chi(k)$ in the R-space using the ARTEMIS module of IFEFFIT4. Effective backscattering amplitudes $F(k)$ and phase shifts $\Phi(k)$ of all fitting paths were calculated by the ab initio code FEFF6.0. In order to fit the curves in the R-range of $1\text{--}4 \text{ \AA}^{-1}$, we considered In-S, and In-In paths as the central-peripheral. For each path, the structural parameters, like coordination number (N), interatomic distance (R), and edge-energy shift (ΔE_0) were opened to be varied.

2.2. Materials and synthesis

2.2.1. Materials

Indium chloride tetrahydrate ($InCl_3\text{-}4H_2O$), Triethanolamine (TEOA) was obtained from Aladdin. Zinc acetate dehydrate ($Zn (CH_3COO)_2\text{-}2H_2O$), thioacetamide (TAA) was purchased from Alfa Aesar. All the chemicals were obtained from commercial sources of analytical reagent (AR) grade without further purification. Deionized water ($18.2 \text{ M}\Omega\text{cm}^{-1}$) was used throughout the experiments.

2.2.2. Synthesis of $Vs\text{-}ZnIn_2S_{4-x}$

0.8 mmol (0.175 g) $Zn (CH_3COO)_2\text{-}2H_2O$, 1.6 mmol (0.469 g) $InCl_3\text{-}4H_2O$, 6.4 mmol (0.481 g) TAA are dissolved in 30 mL H_2O and 30 mL ethanol with ultrasonic dispersion 10 min, and then vigorous stirring for 30 min in room temperature. Then, the mixture solution poured into a Teflon vessel held in a stainless-steel autoclave sealed (100 mL in capability), and heated at 200 °C for 24 h. After cooling to room temperature naturally, the obtained yellow precipitates collected by centrifugation, washing by water and ethanol for several times, and then dried in the vacuum freeze-drying equipment for two days. The obtained yellow powders are denoted as $Vs\text{-}ZnIn_2S_{4-x}$.

2.2.3. Synthesis of $P_4\text{@}Vs\text{-}ZnIn_2S_{4-x}$

$Vs\text{-}ZnIn_2S_{4-x}$ samples were weighed and dispersed in 50 mL of aqueous solution, sonicated well, and then further dispersed for 2 h by a cell wall crusher to obtain a uniformly dispersed yellow solution (1 mg mL $^{-1}$). Then red phosphorus (RP) was added into the obtained solution, which was stirred vigorously at room temperature for 2 h to make it mixed well. The mixed solution was transferred into a reaction kettle (100 mL) with ethylenediamine (ED) (75 mL) and heated at 200 °C for 24 h. After the reaction, the mixed solution was centrifuged several times with water, methanol and ethanol, respectively, to obtain a light pink precipitate. Finally, the collected precipitate was freeze-dried in a vacuum freeze-drying device for 24 h. The obtained samples were labeled as $P_4\text{@}Vs\text{-}ZnIn_2S_{4-x}\text{-}0.5$, $P_4\text{@}Vs\text{-}ZnIn_2S_{4-x}\text{-}1$, $P_4\text{@}Vs\text{-}ZnIn_2S_{4-x}\text{-}1.5$, $P_4\text{@}Vs\text{-}ZnIn_2S_{4-x}\text{-}2$, $P_4\text{@}Vs\text{-}ZnIn_2S_{4-x}\text{-}3$, respectively, where the content of RP input was 50 mg, 100 mg, 150 mg, 200 mg, 350 mg, respectively.

2.3. DFT calculation

The spin polarized DFT calculations were performed using the linear combination of atomic orbitals (LCAO) method. A double numerical polarization (DNP) polarization basis set was used to ensure the accuracy of the calculations. The electron exchange correlation effects are described by the Perdew-Burke-Ernzerhof (PBE) functional at the generalized gradient approximation (GGA) level. A large orbital cutoff of 5 Å and a real-space k-point density below 0.05/Å were chosen to obtain good convergence. The van der Waals (vdW) correction was performed using the TS method. A monolayer ZIS flat model containing

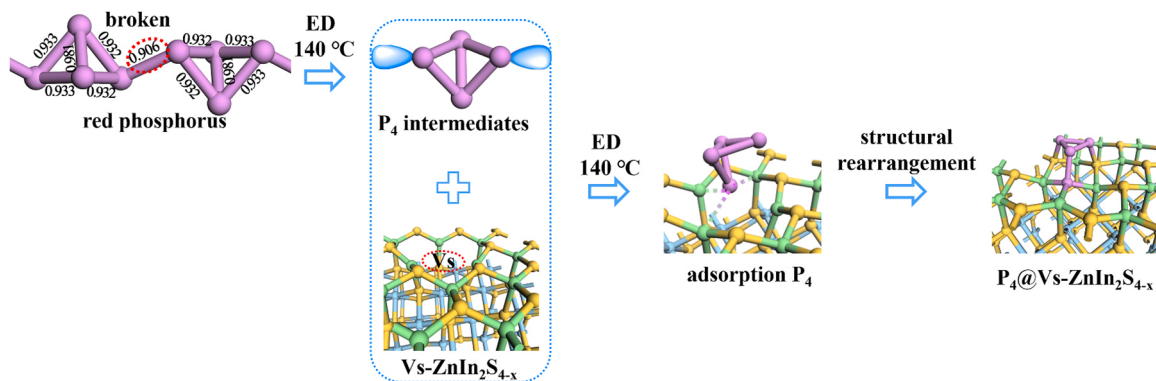


Fig. 1. Proposed formation mechanism of $P_4@Vs\text{-}ZnIn_2S_{4-x}$ in ED solvothermal reaction.

a 15 Å vacuum was used to shield the effect of periodic mirroring, and a $4 \times 4 \times 1$ supercell was employed. To describe the electron-ion interactions, a DFT-based relativistic DFT semi-core pseudopotentials (DSPP) was used. During geometric optimization, all atoms are allowed to relax until the model reaches a ground state without any imaginary frequencies. The convergence criteria for the self-consistent field (SCF) iteration and the maximum force of the model are 10^{-7} Ha and 0.001 Ha/Å, respectively.

2.4. Photocatalytic activity test

Typically, 2 mg of photocatalyst is dispersed in 20 mL aqueous solution containing 25 vol% TEOA as sacrificial electron donor. The photocatalytic reaction is carried out in a closed system with a volume 54 mL (34 mL for calculating H₂ evolution), and the reaction system is bubbled with argon gas through the reactor for 30 min to remove the

dissolved oxygen. A 300 W Xenon lamp is used as a simulated solar light source with a UV-light cutoff filter ($\lambda \geq 420$ nm). The volume of H₂ is measured by a gas chromatograph (SHIMADZU GC-2014, TCD).

3. Results and discussion

3.1. Formation mechanism of $P_4@Vs\text{-}ZnIn_2S_{4-x}$ structure

The $P_4@Vs\text{-}ZnIn_2S_{4-x}$ structure is synthesized with RP and Vs-ZnIn₂S_{4-x} by a simple ED solvothermal process. Classic amorphous RP is a linear chain structure consisting of double triangles [40]. From Mulliken population analysis, the bond order of the linking bonds between double triangles (0.906) is weaker than that of the arbitrary bonds in triangles (0.932, 0.933, or 0.981) (Fig. 1). In ED solution, amino anions were produced by self-ionization. When RP is dissolved in ethylenediamine, the amino anions, acting as nucleophiles, attack the 3d

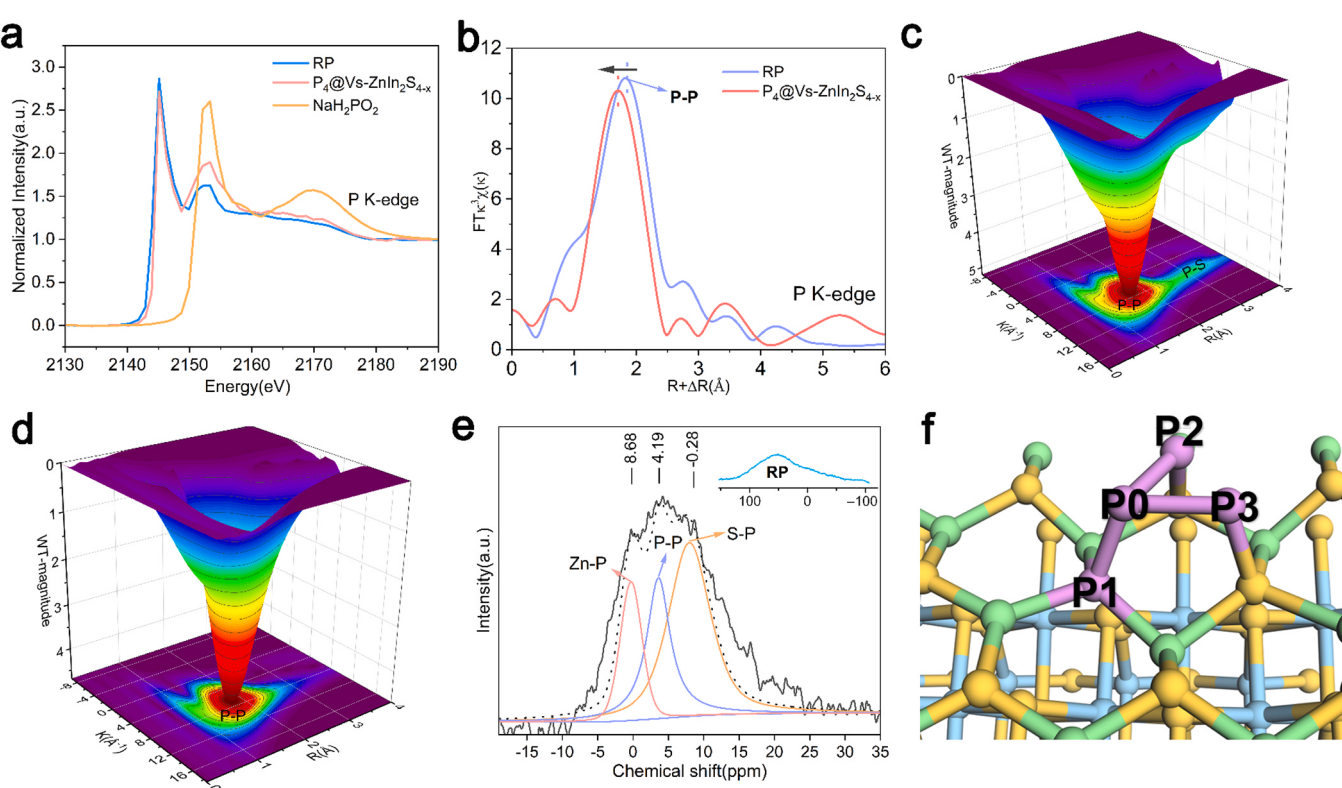


Fig. 2. a) the normalized P K-edge XANES spectra for RP, $P_4@Vs\text{-}ZnIn_2S_{4-x}$ and NaH_2PO_2 , b) P K-edge Fourier transforms k^3 -weighted EXAFS spectra in R space for RP and $P_4@Vs\text{-}ZnIn_2S_{4-x}$, c-d) P K-edge WT contour plots for $P_4@Vs\text{-}ZnIn_2S_{4-x}$ and RP, e) solid-state ³¹P NMR for $P_4@Vs\text{-}ZnIn_2S_{4-x}$, f) structural model of $P_4@Vs\text{-}ZnIn_2S_{4-x}$.

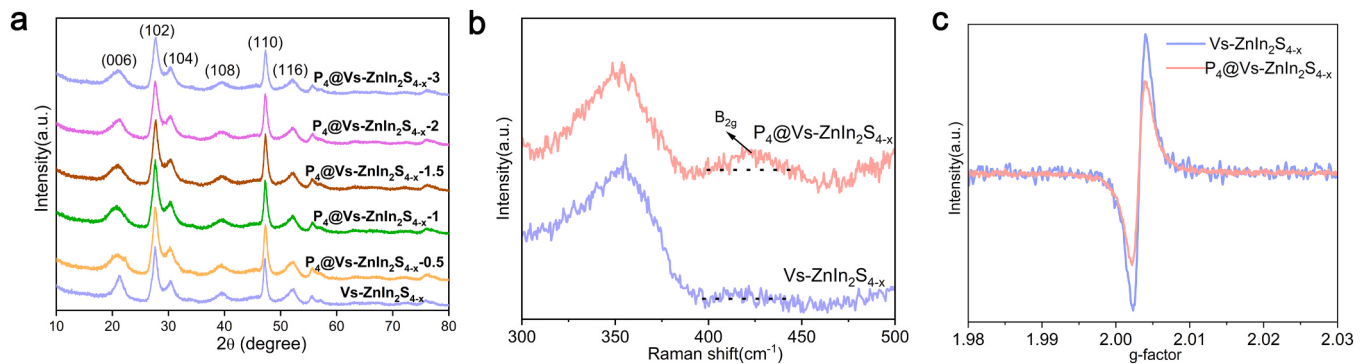


Fig. 3. a) XRD spectra for Vs-ZnIn₂S_{4-x} and P₄@Vs-ZnIn₂S_{4-x} with different RP amount, b) Raman spectra for RP and P₄@Vs-ZnIn₂S_{4-x}, c) EPR spectra for Vs-ZnIn₂S_{4-x} and P₄@Vs-ZnIn₂S_{4-x}.

unoccupied orbitals of RP molecules, inducing the heterolysis of P-P bonds and generating polyphosphorus-amine anions. As a result, the weak linking bond is preferentially broken, and RP decomposes into high-activity P₄ intermediates [41]. The high-active P₄ intermediates tentatively adsorb onto the S-defective site of Vs-ZnIn₂S_{4-x} to reduce the total energy of system through structural rearrangement, forming a stable P₄@Vs-ZnIn₂S_{4-x} structure. Meanwhile, density function theory (DFT) calculations reveal that P₄ molecular anchored on Zn-S₄ surface, rather than In-S₄ surface, is energetically favorable for the lower surface energy (Fig. S1).

3.2. Morphology, structure and surface chemical states

The coordination structure and chemical environment of molecule-semiconductor hybrid P₄@Vs-ZnIn₂S_{4-x} photocatalyst was disclosed by X-ray absorption fine structure (XAFS) measurements. As shown in P K-edge X-ray absorption near-edge structure (XANES) patterns, the P K-edge position of P₄@Vs-ZnIn₂S_{4-x} shifts slightly to the higher energy than reference RP and lowers than that of NaH₂PO₂, suggesting that

valent state of P in P₄@Vs-ZnIn₂S_{4-x} is slightly higher than zero (Fig. 2a). The oxidized P in P₄ @Vs-ZnIn₂S_{4-x} reveals that P-species inject electrons into Vs-ZnIn₂S_{4-x} substrate, which shifts binding energy of Zn, In and S elements towards lower energy (Fig. S2a-c). The P K-edge extended X-ray absorption fine structure (EXAFS) spectra fitting result indicates that the P atoms in P₄@Vs-ZnIn₂S_{4-x} with the bond length of 2.09 Å and 2.31 Å, which correspond to the P-S and P-P scattering contribution, respectively. Obviously, the bond distance of P-P bonds in P₄@Vs-ZnIn₂S_{4-x} is shorter than that of RP (Fig. 2b), demonstrating that P exists in P₄@Vs-ZnIn₂S_{4-x} in the form different from that of RP clusters. Meanwhile, the presence of P-P scattering paths (1.76 Å, 6.92 Å⁻¹) and the P-S scattering paths (3.27 Å, 8.15 Å⁻¹) are further identified in P₄@Vs-ZnIn₂S_{4-x} by EXAFS wavelet transform (WT) analysis, which is distinguish from single P-P scattering paths (1.85 Å, 7.12 Å⁻¹) in RP (Fig. 2c-d). Further, Zn K-edge EXAFS indicates that the distance of Zn-S bond is shortened from 1.95 Å (Vs-ZnIn₂S_{4-x}) to 1.91 Å (P₄@Vs-ZnIn₂S_{4-x}), attributing to the formation of P-Zn bonds in P₄@Vs-ZnIn₂S_{4-x} (Fig. S2d). In addition, the solid-state ³¹P Nuclear Magnetic Resonance (NMR) result indicates the presence of three kinds of P atoms

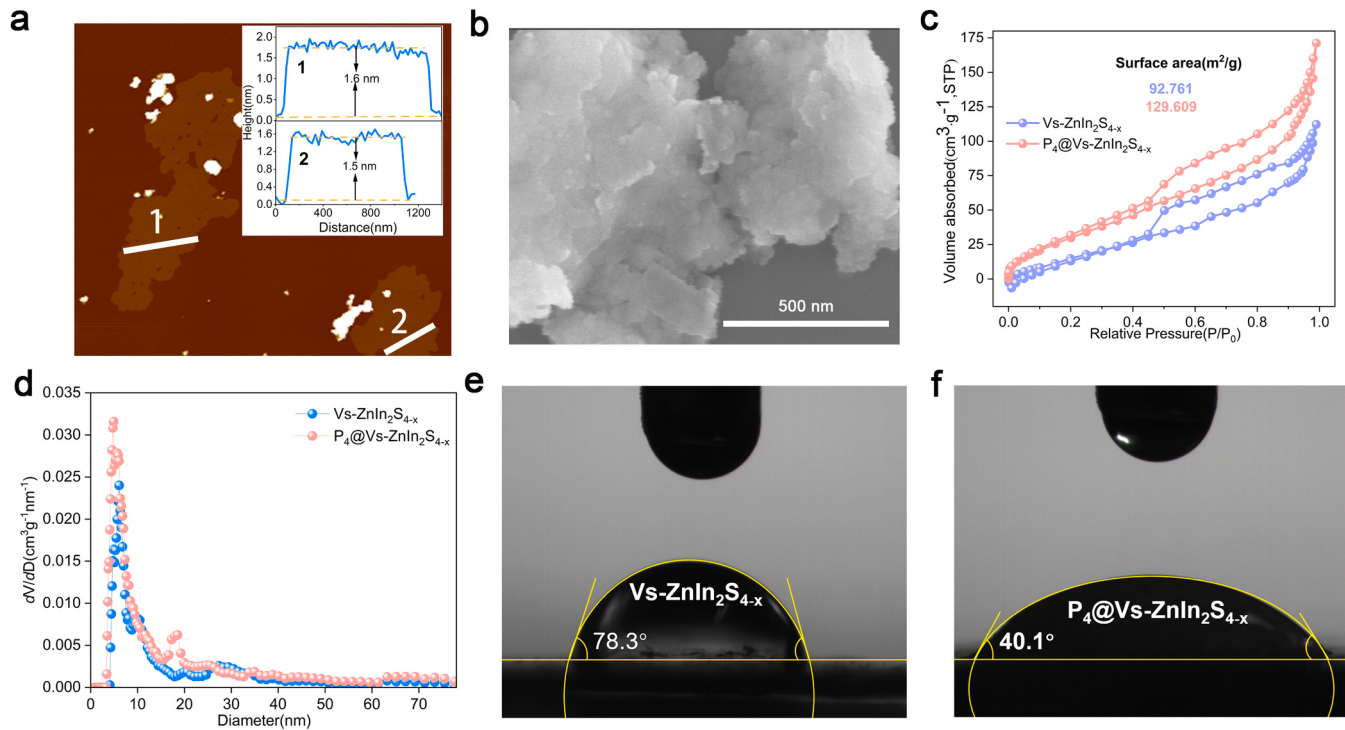


Fig. 4. a) AFM spectra and b) SEM spectra for P₄@Vs-ZnIn₂S_{4-x}, c-d) N₂ adsorption-desorption isotherm and pore size distribution of Vs-ZnIn₂S_{4-x} and P₄@Vs-ZnIn₂S_{4-x}, e-f) Contact angle measurements of Vs-ZnIn₂S_{4-x} and P₄@Vs-ZnIn₂S_{4-x}.

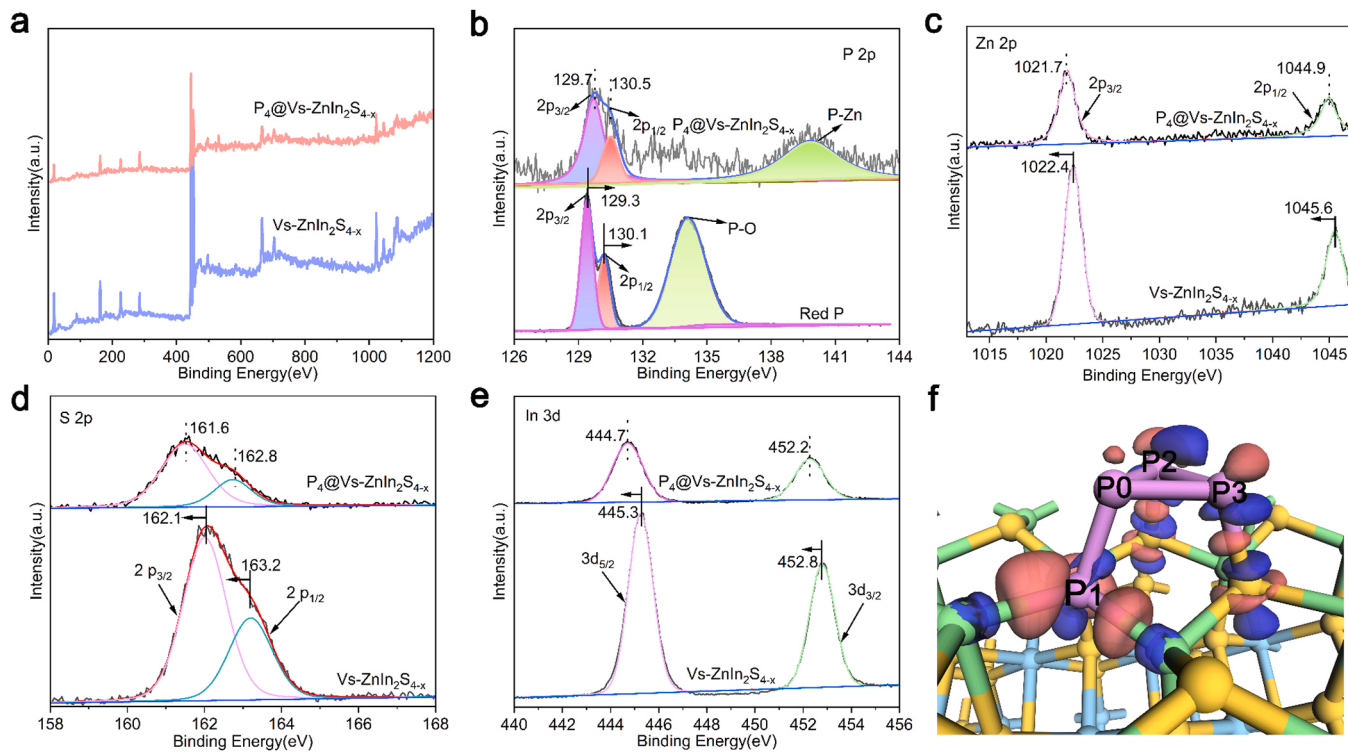


Fig. 5. a) XPS spectra for a survey scan and high-resolution XPS spectra of b) P 2p, c) Zn 2p, d) S 2p, and e) In 3d in Vs-ZnIn₂S_{4-x} and P₄@Vs-ZnIn₂S_{4-x}, (f) Differential charge density diagram of P₄@Vs-ZnIn₂S_{4-x} (blue area represents the electron depletion and pink region means the electron accumulation).

with different chemical environment in P₄@Vs-ZnIn₂S_{4-x}, whose atomic ratio is 1:1:2 from low chemical shift to high chemical shift (Fig. 2e). Since the P NMR signal moves to the high chemical shift when the electron density around P nucleus decrease, the molar ratio of P-Zn bonds, P-P bonds, and P-S bonds is 1:1:2. Overall, the XAFS and ³¹P NMR synergistically analysis reveals that P₄ molecular is anchored to the Zn-S₄ surface through P-Zn and P-S bonds, where the P₀ atom maintains the coordination state of RP, the P₁ atom fills S-defect, P₂ and P₃ atoms bond with S atoms, respectively. So, effective bonding to the substrate is achieved and electrons are well injected into the substrate through P-S bonds, increasing the electron density of nearby S atoms (Fig. 2f).

XRD diffraction peaks of P₄@Vs-ZnIn₂S_{4-x} located 21.6°, 27.2° and 47.3° correspond to (006), (102), (110) facets of hexagonal phase ZnIn₂S₄ (PDF#72-0773), respectively (Fig. 3a), which is similar as that of Vs-ZnIn₂S_{4-x}. No peaks of P compounds were found, indicating the absence of bulk phosphide, while the undetectable characteristic peak shift indicates that P elements did not enter the lattice interior. Meanwhile, the Raman characteristic peak located at 426 cm⁻¹ in P₄@Vs-ZnIn₂S_{4-x} is similar to the B_{2g} vibration mode of typical structures of black phosphorus and shifts to the low wavenumber, indicating the existence of the deformed P₄ structure (Fig. 3b). In addition, both Vs-ZnIn₂S_{4-x} and P₄@Vs-ZnIn₂S_{4-x} exhibit obvious electron paramagnetic resonance (EPR) signals. Especially, the EPR response of P₄@Vs-ZnIn₂S_{4-x} is weaker than that of Vs-ZnIn₂S_{4-x}, indicating that the defect structure of P₄@Vs-ZnIn₂S_{4-x} is filled up at a certain by the P from P₄ (Fig. 3c) [42]. The quantitative analysis of elements shows that the P contents can only up to 0.202 wt%, which is very trace in P₄@Vs-ZnIn₂S_{4-x} (Table S1). Besides, the TEM image (Fig. S3a) reveals that P₄@Vs-ZnIn₂S_{4-x} has regular 2D nanosheets morphology with a very smooth surface. The Zn, In, S and P elements are well distributed on P₄@Vs-ZnIn₂S_{4-x}, and no obvious P nanoparticles (Fig. S3b).

The morphology of molecule-semiconductor hybrid P₄@Vs-ZnIn₂S_{4-x} is homogeneous nanosheets with the thickness of *c.a.* 1.5 nm, while that of Vs-ZnIn₂S_{4-x} is microsphere formed by overlapping of nanosheets (Fig. S4), indicating that the P₄ molecular can effectively

suppress the agglomeration (Fig. 4a-b). In addition, the specific surface area of P₄@Vs-ZnIn₂S_{4-x} increases to 129.7 m² g⁻¹ from 92.8 m² g⁻¹ of Vs-ZnIn₂S_{4-x} and pore size is centralized distribution of 3–20 nm mesoporous (Fig. 4c-d). Dramatic increase in surface area reveals that P₄@Vs-ZnIn₂S_{4-x} can expose abundant active sites to participate in the catalytic reaction. Vs-ZnIn₂S_{4-x} shows a contact angle of 78.3°, suggesting a moderate hydrophilicity of the surface [43] (Fig. 4e). While, the contact angle of P₄@Vs-ZnIn₂S_{4-x} decreases to 40.1° with the introduction of P₄ molecular (Fig. 4f). On the one hand, the P₄ molecules broke the original periodic structure of the Zn-S₄ surface, creating a polar surface. On the other hand, the pristine nonpolar P₄ tetrahedrons were disordered to polar ones because of the strong electronic coupling within P₄ and Zn-S₄ substrates, strengthening interaction with water molecules. Thus, the hydrophilicity of the material is significantly increased.

The chemical composition and bonding environment of the Vs-ZnIn₂S_{4-x} and P₄@Vs-ZnIn₂S_{4-x} were investigated by X-ray photoelectron spectroscopy (XPS). Full scan spectra of Vs-ZnIn₂S_{4-x} and P₄@Vs-ZnIn₂S_{4-x} show obvious signals of Zn, In, S and P elements (Fig. 5a). The characteristic peak of the P-O bond is not detected in P₄@Vs-ZnIn₂S_{4-x}, indicating that the phosphorus is not in the form of phosphorus oxide. The P 2p peaks of P₄@Vs-ZnIn₂S_{4-x} are located at 129.7 eV and 130.5 eV for P 2p_{3/2} and P 2p_{1/2}, respectively, indicating that the valence state of P atoms approximates to the zero-valence state [44] (Fig. 5b), which is consistent with the XAFS results (Fig. 2a). Consistent with solid-state NMR results, the P 2p peak at 140 eV is attributed to the Zn-P bond, further proving that the P₄ molecule is anchored on the [ZnS]₄ surface in P₄@Vs-ZnIn₂S_{4-x}. For Vs-ZnIn₂S_{4-x}, the peak at 1022.4 eV and 1045.6 eV correspond to Zn 2p binding energy, the S 2p peak is split into 2p_{1/2} (163.2 eV) and 2p_{3/2} (162.1 eV), and the binding energy of In 3d_{3/2} and In 3d_{5/2} are located to 452.8 eV and 445.3 eV (Fig. 5c-e) [27]. Interestingly, the binding energy of Zn atoms, In atoms and S atoms in P₄@Vs-ZnIn₂S_{4-x} display a negative shift relative to Vs-ZnIn₂S_{4-x}, and the binding energy of P atoms in P₄@Vs-ZnIn₂S_{4-x} display a positive shift relative to RP [45]. The shift of binding energy

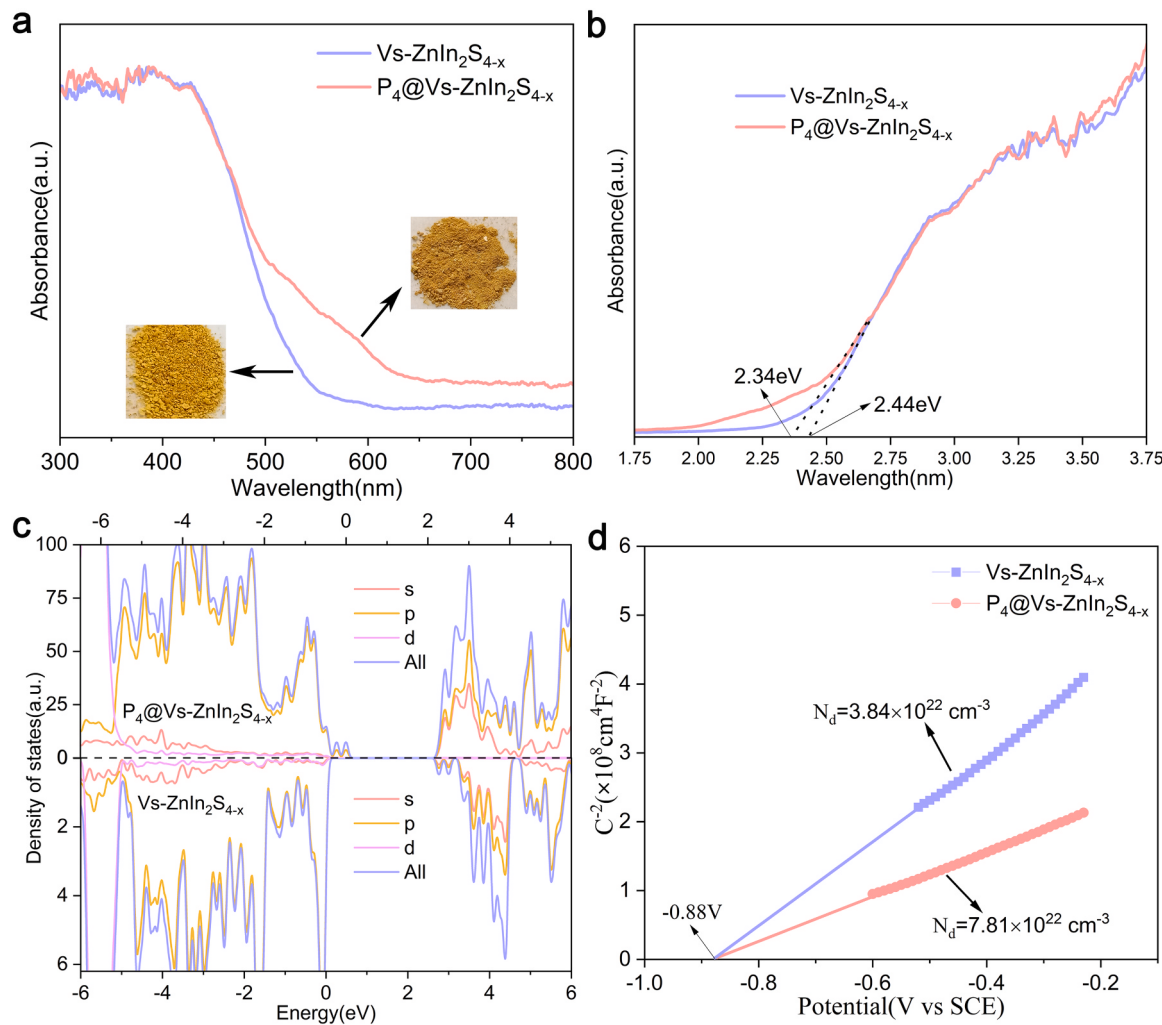


Fig. 6. a) UV-vis DRS spectra, b) band gap that estimated by a related curve of $(\alpha h\nu)^{1/2}$ versus photon energy plotted, c) calculated density of states, d) Mott-Schottky plots of Vs-ZnIn₂S_{4-x} and P₄@Vs-ZnIn₂S_{4-x}.

provides the electron transfer from P₄ molecular to Vs-ZnIn₂S_{4-x} [46], which is consistent with the XAFS result (Fig. 2a). Further, the charge density difference calculation certifies the electron redistribution at the interface between P₄ and Vs-ZnIn₂S_{4-x} (electron flow from P₄ to Vs-ZnIn₂S_{4-x}) (Fig. 5f), which demonstrates strong electronic coupling and further reveals the polarity of the surface.

3.3. Photoelectrochemical characteristics and kinetic behavior of carriers

The ultraviolet-visible diffuse reflectance spectroscopy (UV-vis DRS) was performed to investigated the optical absorption properties of Vs-ZnIn₂S_{4-x} and P₄@Vs-ZnIn₂S_{4-x}. The Vs-ZnIn₂S_{4-x} possess the photo-absorption region from UV light to visible light and the absorption edge is located at 508 nm in visible region. The light absorption curves of P₄@Vs-ZnIn₂S_{4-x} exhibits significant redshift and appears the additional absorption peak (Fig. 6a). The additional absorption signal at 500–600 nm is attributed to the presence of strong interactions between P₄ molecules and the Vs-Zn₂S_{4-x} surface. The formed P-Zn and P-S bonds triggered a change of the local surface chemical environment, which not only increased the density of states near the Fermi level, but also induced impurity energy levels at the top of the valence band. Specifically, UV-vis DRS reveals that P₄ molecular can effectively short band gap and promote the light-harvesting capability of pristine Vs-ZnIn₂S_{4-x} (Fig. 6b). Moreover, since the electronic coupling between the P₄ molecule and Vs-ZnIn₂S_{4-x}, the orbitals with low density of states at the

conduction band minimum (CBM) is pushed to around valence band maximum (VBM) (Fig. S5), and the CBM is dominated by the orbitals with high density of states, significantly increasing the ability of the CBM to accommodate photogenerated electrons and suggesting that more charge carriers can participate in the photocatalytic reaction (Fig. 6c). Furthermore, P₄ molecular induces the additional diffusive electronic states on the top of the valence band [47], which narrows bandgap and increases the carrier concentration (Figs. S6–7). Moreover, calculated from the Mott-Schottky results, the carrier density (N_d) of P₄@Vs-ZnIn₂S_{4-x} ($7.81 \times 10^{22} \text{ cm}^{-2}$) is increased 2.04-fold relative to that of Vs-ZnIn₂S_{4-x} ($3.84 \times 10^{22} \text{ cm}^{-2}$) (Fig. 6d).

The behavior of carrier separation is further investigated. Vs-ZnIn₂S_{4-x} exhibits strong photoluminescence (PL) emission at about 400 nm, indicating the presence of serious recombination of electron-hole pairs (Fig. S8). The significantly weakened luminescence of P₄@Vs-ZnIn₂S_{4-x} reveals that P₄ molecular improve the charge separation efficiency via an enhanced electron transfer channel from Vs-ZnIn₂S_{4-x} to P₄ molecular [48]. To further reveal the relaxation process of excited electrons, the ultrafast transient absorption spectroscopy (TA) upon 380 nm laser excitation is performed to probe photogenerated carriers' dynamics in real time [18,49]. Vs-ZnIn₂S_{4-x} generates the broad absorption band in the range of 500–700 nm due to the absorption signal from excited state electron transition (Fig. 7a) [50,51]. The relative change in optical density (COD) of P₄@Vs-ZnIn₂S_{4-x} is more significant than that of Vs-ZnIn₂S_{4-x}, indicating that a higher density of

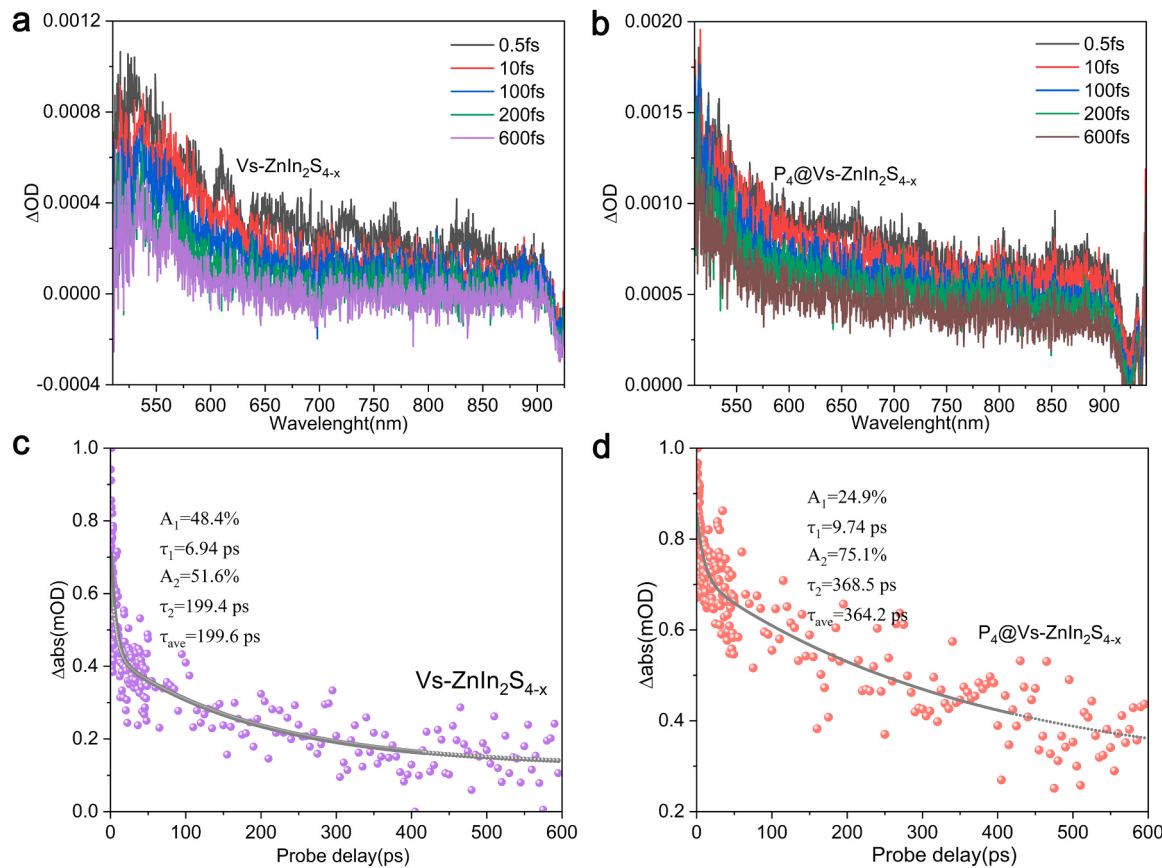


Fig. 7. TA of a) Vs-ZnIn₂S_{4-x} and b) P₄@Vs-ZnIn₂S_{4-x} at different time delays under excitation of 380 nm laser pulses, normalized TA profiles probed at 600 nm for c) Vs-ZnIn₂S_{4-x} and d) P₄@Vs-ZnIn₂S_{4-x}.

the excited carrier in P₄@Vs-ZnIn₂S_{4-x} (Fig. 7b). Further, the TA decay profiles of Vs-ZnIn₂S_{4-x} and P₄@Vs-ZnIn₂S_{4-x} are probed at 600 nm by a two-exponential function. Two-time constants are $\tau_1 = 6.9$ ps (48.4 %) and $\tau_2 = 199.4$ ps (51.6 %) for P₄@Vs-ZnIn₂S_{4-x}, while $\tau_1 = 9.8$ ps (24.9 %) and $\tau_2 = 368.5$ ps (75.1 %) for Vs-ZnIn₂S_{4-x} (Fig. 7c-d). The fast decay component τ_1 , corresponding to the trapped electrons from conduction band into trap states within the bandgap, is nearly not altered. The much slower relaxation process τ_2 , reflecting the recombination between the electrons captured by trap states and the valence band holes, is substantially increased to 368.5 ps of P₄@Vs-ZnIn₂S_{4-x} from 199.4 ps of Vs-ZnIn₂S_{4-x}. The significantly increased τ_2 indicates that the trap states induced by the P₄ molecule capture photogenerated electrons to prolong the carrier's lifetime. Furthermore, the average recovery lifetime of P₄@Vs-ZnIn₂S_{4-x} ($\tau_{ave}=364.2$ ps) is roughly 1.82 times longer than that of Vs-ZnIn₂S_{4-x} ($\tau_{ave}=199.6$ ps), indicating that the P₄ molecular increases separation efficiency of photoexcited carriers and offer more opportunities for the photocatalytic hydrogen production reactions.

The electrochemical measurements were conducted to analyze the carrier's separation and transition efficiency systematically. The outwardly extending electron cloud of P₄ molecule suggests that it will overlap sufficiently with that of ZnIn₂S₄. Further, the slightly small electronegativity of P element means that the electrons of P atoms will transfer to the S atoms. Electron density difference results confirm that the electron density of the S atoms at the P-S bond are significantly higher than that of the other S atoms. Moreover, the weak polarity of the S-Zn bonds near the anchor point (marked by the dotted line) indicates a high degree of delocalization, which promotes the electron transport (Fig. 8a). The delocalized electron can not only be easily excited to participate in the reaction, but also improve the conductivity of P₄@Vs-ZnIn₂S_{4-x}. Moreover, the P₄@Vs-ZnIn₂S_{4-x} presents a smaller initial

potential ($E = -0.43$ V) than Vs-ZnIn₂S_{4-x} ($E = -0.6$ V), attributed to the reduced activation energy and accelerated kinetics after P₄ molecular anchored Zn-S plane (Fig. 8b)[52]. Furthermore, the smaller circular diameter of electrochemical impedance spectroscopy (EIS) Nyquist plot of P₄@Vs-ZnIn₂S_{4-x} than that of Vs-ZnIn₂S_{4-x}, indicating that the anchored P₄ molecule effectively promotes the interfacial charge transfer resistance (Fig. 8c). Specifically, the P₄ molecule injects electrons into the Vs-ZnIn₂S_{4-x} after forming a heterojunction with the Vs-ZnIn₂S_{4-x}, which creates a built-in electric field pointing from P₄ to Vs-ZnIn₂S_{4-x} and induces an electrostatic potential depression in the Vs-ZnIn₂S_{4-x} plane. These effects synergistically enhance the electron transport. On the other hand, the P₄ molecules anchoring to the Vs-ZnIn₂S_{4-x} surface distort themselves into polar molecules, which substantially improves the compatibility of the material with water (as evidenced by the contact angle test) and facilitates the electron transfer from the material to the liquid phase. Meanwhile, P₄ molecule improve the charge separation efficiency, and thus P₄@Vs-ZnIn₂S_{4-x} exhibits higher transient photocurrent density than Vs-ZnIn₂S_{4-x} (Fig. 8d). All of photoelectrochemical measurements indicate that the P₄ molecular indeed accelerate surface reaction kinetics by promoting carrier's separation and transition.

3.4. Photocatalytic hydrogen evolution activity

The photocatalytic H₂ production activity of the Vs-ZnIn₂S_{4-x} and P₄@Vs-ZnIn₂S_{4-x} are evaluated under visible light irradiation ($\lambda > 420$ nm) with triethanolamine (TEOA) as hole scavenger. The apparent quantum efficiency (AQE) obviously decreased as the light wavelength increased, confirming that photocatalytic hydrogen evolution is photo-driven reaction (Fig. 9a). The Vs-ZnIn₂S_{4-x} is potential photocatalyst with the hydrogen evolution rate of 4.2 mmol g⁻¹ h⁻¹

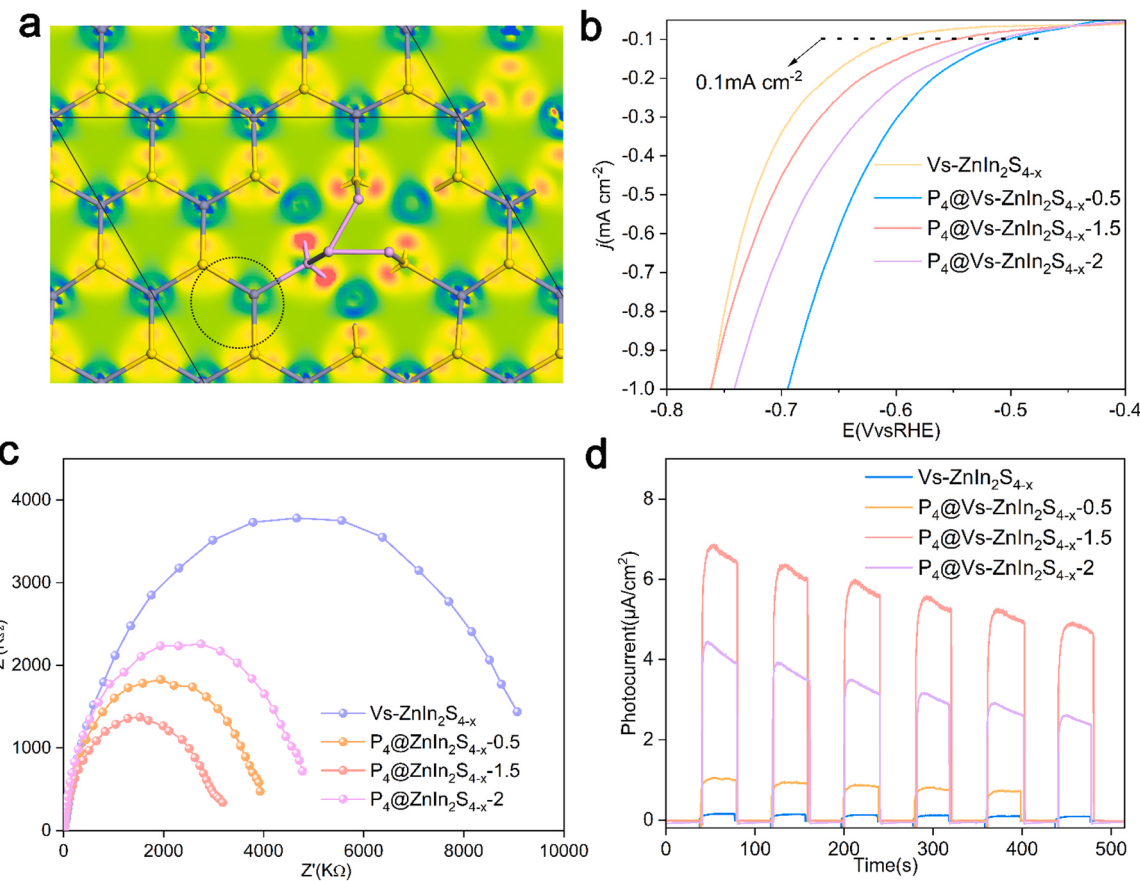


Fig. 8. a) Sectional view of electron difference density of $P_4@Vs\text{-ZnIn}_2\text{S}_{4-x}$, b) LSV curves, c) EIS Nyquist plots and d) transient photocurrent responses for $Vs\text{-ZnIn}_2\text{S}_{4-x}$ and $P_4@Vs\text{-ZnIn}_2\text{S}_{4-x}$ with different RP amount.

(Fig. 9b). Excitingly, the P_4 molecular can realize significantly improved of photocatalytic activity with hydrogen evolution rate of 9.9, 19.1, 26.1, 23.9 and 21.4 $\text{mmol g}^{-1} \text{h}^{-1}$ for the $P_4@Vs\text{-ZnIn}_2\text{S}_{4-x}\text{-}0.5$, $P_4@Vs\text{-ZnIn}_2\text{S}_{4-x}\text{-}1$, $P_4@Vs\text{-ZnIn}_2\text{S}_{4-x}\text{-}1.5$, $P_4@Vs\text{-ZnIn}_2\text{S}_{4-x}\text{-}2$ and $P_4@Vs\text{-ZnIn}_2\text{S}_{4-x}\text{-}3$, respectively [53]. The optimized hydrogen evolution rate of $P_4@Vs\text{-ZnIn}_2\text{S}_{4-x}\text{-}1.5$ can reach up to 26.1 $\text{mmol g}^{-1} \text{h}^{-1}$, which is 6.2 times higher than that of $Vs\text{-ZnIn}_2\text{S}_{4-x}$. However, the excess P_4 molecules are unfavorable. Considering that the surface S defect sites are anchor points of P_4 molecules, if the amount of P_4 is too much, the excess P may exist as clusters on the $P_4@Vs\text{-ZnIn}_2\text{S}_{4-x}$ surface. The P clusters do not have the size advantage of P_4 molecules. The redundant P atoms lead to a strong shading effect, which not only obscures the active site of $Vs\text{-ZnIn}_2\text{S}_{4-x}$, but also hinders the light utilization of $Vs\text{-ZnIn}_2\text{S}_{4-x}$. Therefore, the excess P_4 molecules will inhibit the catalytic activity of the catalyst[54]. The H_2 evolution amount of $P_4@Vs\text{-ZnIn}_2\text{S}_{4-x}$ (1.764 mmol) is 9.9 times higher than $Vs\text{-ZnIn}_2\text{S}_{4-x}$ (0.179 mmol) after 18 h of continuous visible light irradiation, which verifies the sustained hydrogen production ability of $P_4@Vs\text{-ZnIn}_2\text{S}_{4-x}$ (Fig. 9c). The $P_4@Vs\text{-ZnIn}_2\text{S}_{4-x}$ still maintains a high photocatalytic activity after 18 h continuous reaction, and the crystal structure of recycled $P_4@Vs\text{-ZnIn}_2\text{S}_{4-x}$ are similar as those of fresh ones (Fig. 9d). EPR and XPS results also confirm that $P_4@Vs\text{-ZnIn}_2\text{S}_{4-x}$ exhibits remarkable photochemical stability.

3.5. Photocatalytic reaction mechanism

The internal electric field has a significant effect on the distribution and migration direction of carriers [55]. The unique periodic electrostatic potential of ZnIn_2S_4 causes vertical transmission of electron-hole pairs, which results in the fast recombination of photogenerated

carriers in bulk ZnIn_2S_4 [42]. The P_4 molecule is electron-rich compared to $Vs\text{-ZnIn}_2\text{S}_{4-x}$. When the P_4 molecules are anchored on the surface of $Vs\text{-ZnIn}_2\text{S}_{4-x}$, the electrons of P_4 molecules are injected into the $Vs\text{-ZnIn}_2\text{S}_{4-x}$ substrate for the enhanced electronegativity of S atoms respect to P atoms. Thus, the electric field from P_4 molecules pointing toward $Vs\text{-ZnIn}_2\text{S}_{4-x}$ is created, which induces an electrostatic potential depression on the surface of $Vs\text{-ZnIn}_2\text{S}_{4-x}$ (Fig. 10a). The low-potential region acts as the electron vortex to cluster in-plane carriers to P_4 molecular, which weakens vertical transmission of electrons, so as to realize the regulation of the carrier distribution in the Zn-S plane [31]. It is well known that the excellent material for hydrogen evolution reaction (HER) requires a nearly-zero adsorption free energy of H (ΔG_H^0) to compromise the reaction barriers of adsorption and desorption [23]. The ΔG_H^0 on different reaction sites of $Vs\text{-ZnIn}_2\text{S}_{4-x}$ and $P_4@Vs\text{-ZnIn}_2\text{S}_{4-x}$ are calculated to further reveal the kinetics of hydrogen evolution reaction. For $Vs\text{-ZnIn}_2\text{S}_{4-x}$, the calculated ΔG_H^0 of S sites around S vacancies in Zn-S facet is -1.72 eV , demonstrating that the S site of the Zn-S facet has a strong adsorption capacity for H and is chemical inertness. ZnIn_2S_4 heterogenized with black phosphorus owns optimized the adsorption/desorption strength of H intermediate, but it is not ideal ($\Delta G_H^0 = -0.46 \text{ eV}$). Whereas, four types of H adsorption sites were existed in Zn-S facet of $P_4@Vs\text{-ZnIn}_2\text{S}_{4-x}$, which can be classified as S adsorption sites and P adsorption sites. The structural model of the H atom adsorbed on different sites around P_4 molecular (P_0 , $P_{2,3}$, S_1 and S_2) is illustrated (Fig. S9) and the corresponding ΔG_H^0 are calculated (Fig. 10b). The P_0 site ($\Delta G_H^0 = 0.29 \text{ eV}$) and $P_{2,3}$ site ($\Delta G_H^0 = 0.52 \text{ eV}$) exhibit better optimal hydrogen desorption property as compared to $Vs\text{-ZnIn}_2\text{S}_{4-x}$, suggesting that the superior adsorption and desorption properties of phosphorus species is inherited in $P_4@Vs\text{-ZnIn}_2\text{S}_{4-x}$. The ΔG_H^0 value of S_1 (-0.08 eV) site and S_2 (0.007 eV) site are very close to

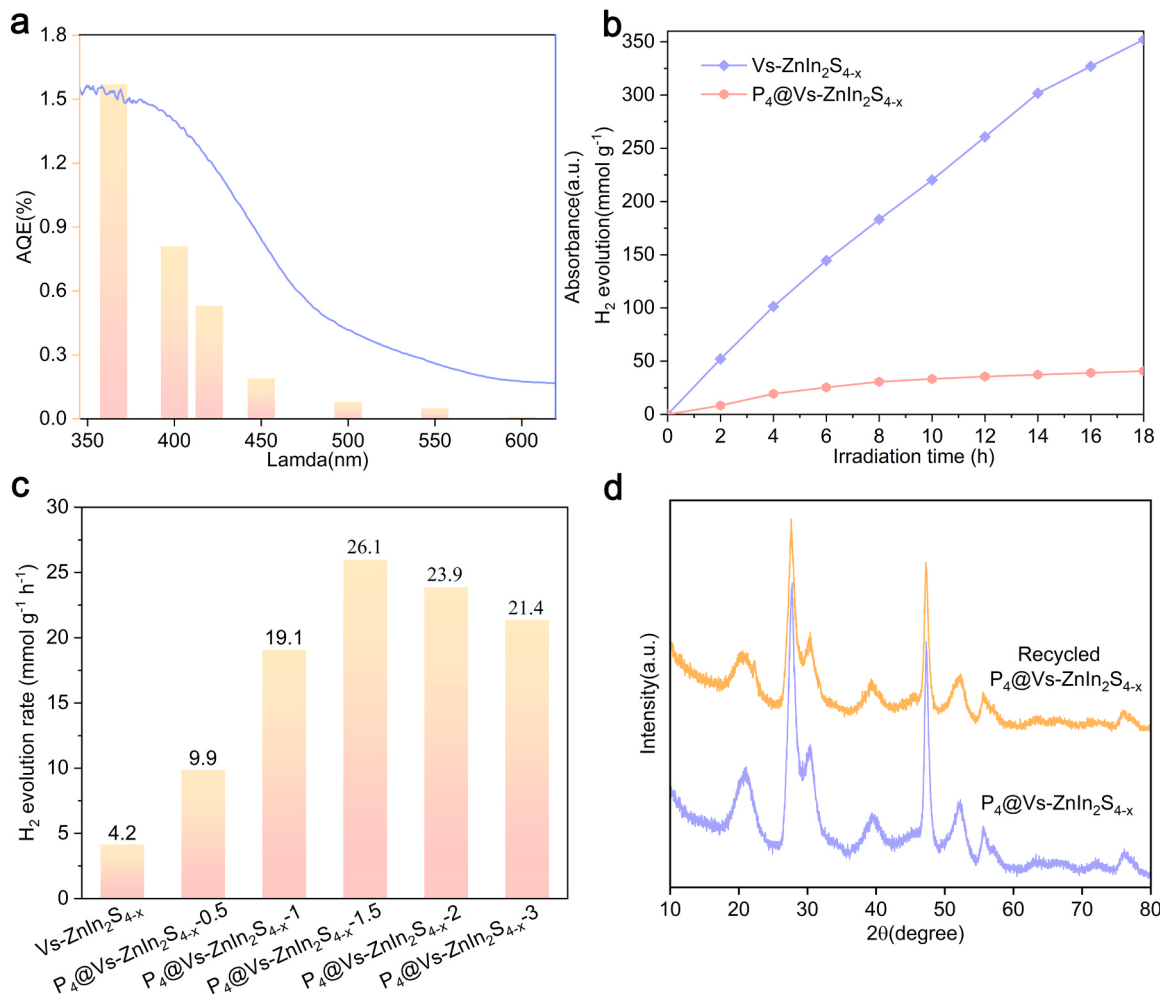


Fig. 9. a) Wavelength dependence of the hydrogen evolution, b) the long-term stability of photocatalytic activity, c) photocatalytic hydrogen evolution reaction activities of different catalysts, d) X-ray diffraction pattern for pristine P₄@Vs-ZnIn₂S_{4-x} and recycled P₄@Vs-ZnIn₂S_{4-x}.

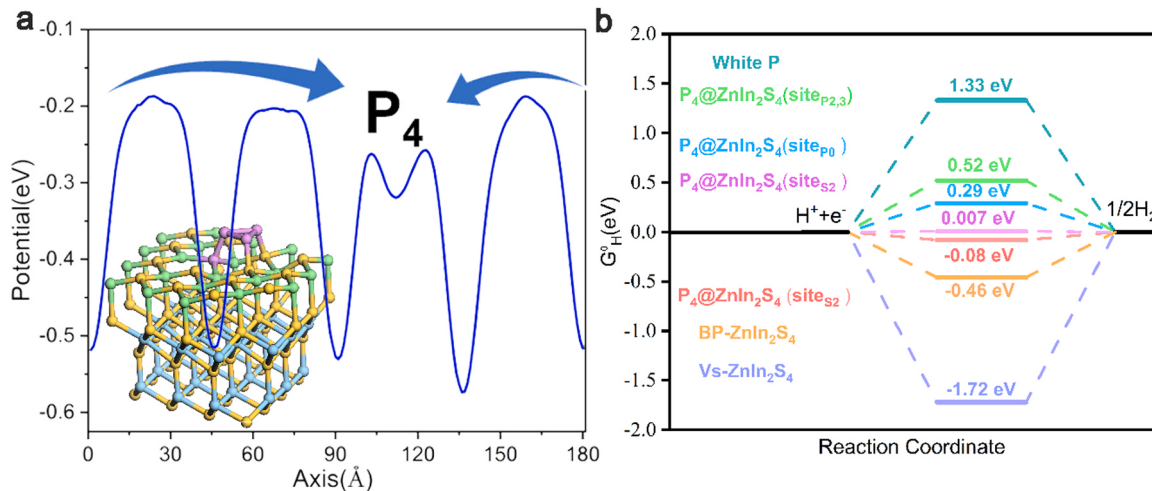


Fig. 10. a) electrostatic potential of P₄@Vs-ZnIn₂S_{4-x} in the direction of [001], b) The calculated Gibbs free-energy (ΔG_H⁰) for chemical absorption of H* on absorption sites near P₄ molecular.

zero, even better than that of the precious metal Pt, which indicates that the S atoms located in inert Zn-S basal plane are activated. This phenomenon is attributed to the electron injection from P₄ molecule into the Zn-S basal plane, which increases the charge density near the S atom,

decreases the attraction of the S atom to the electrons of the H intermediate and weakens the adsorption strength of the H intermediate on S active site. The three-coordinate honeycomb structure of P atoms endow themselves abundant electron cloud density that will inject electrons

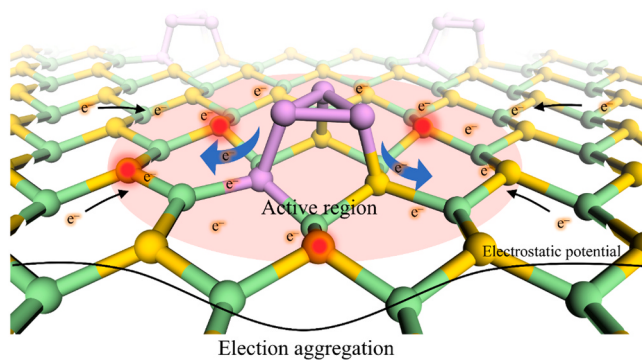


Fig. 11. Schematic illustration of $P_4@Vs\text{-}ZnIn_2S_{4-x}$ nanosheets for photocatalytic H_2 generation reaction.

into the $Vs\text{-}ZnIn_2S_{4-x}$ substrate (Fig. 4f), thus optimizing the H adsorption properties of the S atom on the inert $Zn\text{-}S$ plane [56,57].

The photogenerated electrons are gathered to around P_4 molecular with lower surface electrostatic potential in photocatalytic reaction. Meanwhile, the P_4 molecule and the nearby S -site ($P_0, P_{2,3}, S_1$ and S_2) have excellent kinetics of hydrogen evolution. Therefore, the hydrogen evolution reaction can occur simultaneously on P_4 molecule and the nearby S sites (Fig. 11). In summary, P_4 molecule anchored on $Vs\text{-}ZnIn_2S_{4-x}$ can optimize the hydrogen adsorption/desorption on active site, while can gather the in-plane carriers into highly active regions, thus greatly improving the hydrogen evolution kinetics of materials.

4. Conclusion

Molecular co-catalysts with unique size advantage reduces the shading of the active site and provides abundant self-active position, thus ensuring that the host catalyst has sufficient light absorption and active sites. Herein, a novel molecule-semiconductor hybrid $P_4@Vs\text{-}ZnIn_2S_{4-x}$ nanosheets was designed and synthesized for the first time, in which the strong electronic coupling between the P_4 molecule and $Vs\text{-}ZnIn_2S_{4-x}$ substrate effectively activates the inert $Zn\text{-}S_4$ surface of ZIS and generates an electrostatic potential depression that drives the migration of electrons to active site. $P_4@Vs\text{-}ZnIn_2S_{4-x}$ photocatalyst exhibits excellent hydrogen evolution rate of $26.1\text{ mmol g}^{-1}\text{ h}^{-1}$, which is six times higher than that of $Vs\text{-}ZnIn_2S_{4-x}$ ($4.2\text{ mmol g}^{-1}\text{ h}^{-1}$) under visible-light irradiation. The $P_4@Vs\text{-}ZnIn_2S_{4-x}$ exhibits excellent dispersity and hydrophilicity, providing abundant of catalytic sites for photocatalytic reactions. At the same time, the trap states induced by P_4 molecule increase the carrier concentration near the Fermi energy level and capture photogenerated electrons to prolong the carrier's lifetime. DFT calculations demonstrate that the electron-rich P_4 molecular injects electrons into the $Vs\text{-}ZnIn_2S_{4-x}$ substrate, activating the catalytic activity of the S atoms in the $Zn\text{-}S$ inert base plane. Meanwhile, the P_4 molecular induces the low surface electrostatic potential region in the $Zn\text{-}S$ interarea, which gather in-plane electrons to the highly active P_4 molecules. This work successfully realizes the synergistic effect of in-plane carrier distribution and hydrogen evolution kinetics to improve the hydrogen evolution rates, which provides a new idea for the design of novel molecular-type cocatalysts.

CRediT authorship contribution statement

Wenjun Dong designed the light-facilitated structure reconstruction on self-optimized photocatalyst, and revised the paper. **Qingjie Luan** conducted structure design, experiments, characterization, analysis, and paper writing. **Xiangdong Xue** performed structure design and theoretical calculation. **Tengfei Chen** and **Mengxi Tan** performed experimental characterization and analysis. **Dongxue Zhou** performed experiments and analysis. All authors contributed to the interpretation

of the results and improvement of the paper.

Declaration of Competing Interest

The authors declare that they have no known competing financial interests or personal relationships that could have appeared to influence the work reported in this paper.

Data availability

Data are available from the corresponding authors upon reasonable request.

Acknowledgements

This work was supported by the National Natural Science Foundation of China (52071027, 51872025), the Beijing Municipal Natural Science Foundation (2212038), Natural Science Foundation of Guangdong Province (2022A1515011852), the National Defense Basic Scientific Research (JCKY2022208B002, JCKY2021110B206), Scientific and Technological Innovation Foundation of Foshan (BK21BE008, BK22BE008) for financial support. The computing work is supported by USTB MatCom of Beijing Advanced Innovation Center for Materials Genome Engineering.

Appendix A. Supporting information

Supplementary data associated with this article can be found in the online version at [doi:10.1016/j.apcatb.2023.122932](https://doi.org/10.1016/j.apcatb.2023.122932).

References

- [1] P. Wang, Z. Shen, Y. Xia, et al., Atomic insights for optimum and excess doping in photocatalysis: a case study of few-layer Cu-ZnIn₂S₄, *Adv. Funct. Mater.* 29 (3) (2019) 1807013.
- [2] R. Chattot, O. Le Bacq, V. Beermann, et al., Surface distortion as a unifying concept and descriptor in oxygen reduction reaction electrocatalysis, *Nat. Mater.* 17 (9) (2018) 827–833.
- [3] J. Li, X. Wu, W. Pan, et al., Vacancy-rich monolayer BiO²⁻_x as a highly efficient UV, visible, and near-infrared responsive photocatalyst, *Angew. Chem. Int. Ed.* 57 (2) (2018) 491–495.
- [4] Y. Wang, X. Liu, J. Liu, et al., Carbon quantum dot implanted graphite carbon nitride nanotubes: excellent charge separation and enhanced photocatalytic hydrogen evolution, *Angew. Chem.* 130 (20) (2018) 5867–5873.
- [5] H. Wu, H.L. Tan, C.Y. Toe, et al., Photocatalytic and photoelectrochemical systems: similarities and differences, *Adv. Mater. Interfaces* 32 (18) (2020) 1904717.
- [6] X. Dang, M. Xie, F. Dai, et al., Ultrathin 2D/2D ZnIn₂S₄/g-C₃N₄ nanosheet heterojunction with atomic-level intimate interface for photocatalytic hydrogen evolution under visible light, *Adv. Mater. Interfaces* 8 (10) (2021) 2100151.
- [7] R. Li, Q. Luan, C. Dong, et al., Light-facilitated structure reconstruction on self-optimized photocatalyst TiO₂/BiOCl for selectively efficient conversion of CO₂ to CH₄, *Appl. Catal. B: Environ.* 286 (2021), 119832.
- [8] F. Fang, Y. Liu, X. Sun, et al., TiO₂ Facet-dependent reconstruction and photocatalysis on CuO_x/TiO₂ photocatalysts in CO₂ photoreduction, *Appl. Surf. Sci.* 564 (2021), 150407.
- [9] X. Wang, G. Hai, B. Li, et al., Construction of dual-Z-scheme WS₂-WO₃-H₂O/g-C₃N₄ catalyst for photocatalytic H₂ evolution under visible light, *Chem. Eng. J.* 426 (2021), 130822.
- [10] M. Tan, Y. Ma, C. Yu, et al., Boosting photocatalytic hydrogen production via interfacial engineering on 2D ultrathin Z-scheme ZnIn₂S₄/g-C₃N₄ heterojunction, *Adv. Funct. Mater.* (2021) 2111740.
- [11] X. Wang, X. Wang, J. Huang, et al., Interfacial chemical bond and internal electric field modulated Z-scheme Sv-ZnIn₂S₄/MoSe₂ photocatalyst for efficient hydrogen evolution, *Nat. Commun.* 12 (1) (2021) 1–11.
- [12] Q. Luan, X. Xue, R. Li, et al., Boosting photocatalytic hydrogen evolution: orbital redistribution of ultrathin ZnIn₂S₄ nanosheets via atomic defects, *Appl. Catal. B: Environ.* 305 (2022), 121007.
- [13] P. Chen, Y. Zhou, F. Dong, Advances in regulation strategies for electronic structure and performance of two-dimensional photocatalytic materials, *Acta Phys. -Chim. Sin.* 37 (8) (2021) 2010010.
- [14] X. Zhong, K.-X. Zhang, D. Wu, et al., Enhanced photocatalytic degradation of levofloxacin by Fe-doped BiOCl nanosheets under LED light irradiation, *Chem. Eng. J.* 383 (2020), 123148.
- [15] J. Zhong, Y. Zhao, L. Ding, et al., Opposite photocatalytic oxidation behaviors of BiOCl and TiO₂: direct hole transfer vs. indirect OH oxidation, *Appl. Catal. B: Environ.* 241 (2019) 514–520.

[16] M. Zhu, G. Diao, High catalytic activity of CuO nanorods for oxidation of cyclohexene to 2-cyclohexene-1-one, *Catal. Sci. Technol.* 2 (1) (2012) 82–84.

[17] W. Li, Z. Lin, G. Yang, A 2D self-assembled MoS₂/ZnIn₂S₄ heterostructure for efficient photocatalytic hydrogen evolution, *Nanoscale* 9 (46) (2017) 18290–18298.

[18] W. Yang, L. Zhang, J. Xie, et al., Enhanced photoexcited carrier separation in oxygen-doped ZnIn₂S₄ nanosheets for hydrogen evolution, *Angew. Chem. Int. Ed.* 55 (23) (2016) 6716–6720.

[19] X. Jiao, Z. Chen, X. Li, et al., Defect-mediated electron-hole separation in one-unit-cell ZnIn₂S₄ layers for boosted solar-driven CO₂ reduction, *J. Am. Chem. Soc.* 139 (22) (2017) 7586–7594.

[20] J. Qin, Q. Zhao, Y. Zhao, et al., Metal-free phosphorus-doped ZnIn₂S₄ nanosheets for enhanced photocatalytic CO₂ reduction, *J. Phys. Chem. C* 125 (43) (2021) 23813–23820.

[21] G. Zuo, Y. Wang, W.L. Teo, et al., Ultrathin ZnIn₂S₄ nanosheets anchored on Ti₃C₂TX MXene for photocatalytic H₂ evolution, *Angew. Chem.* 132 (28) (2020) 11383–11388.

[22] Z. Xiong, Y. Hou, R. Yuan, et al., Hollow NiCo₂S₄ nanospheres as a cocatalyst to support ZnIn₂S₄ nanosheets for visible-light-driven hydrogen production, *Acta Phys. -Chim. Sin.* 38 (7) (2022) 2111021.

[23] X. Shi, L. Mao, P. Yang, et al., Ultrathin ZnIn₂S₄ nanosheets with active (110) facet exposure and efficient charge separation for cocatalyst free photocatalytic hydrogen evolution, *Appl. Catal. B: Environ.* 265 (2020), 118616.

[24] C. Du, B. Yan, G. Yang, Self-integrated effects of 2D ZnIn₂S₄ and amorphous Mo₂C nanoparticles composite for promoting solar hydrogen generation, *Nano Energy* 76 (2020), 105031.

[25] S. Wang, Y. Wang, S.L. Zhang, et al., Supporting ultrathin ZnIn₂S₄ nanosheets on Co/N-Doped graphitic carbon nanocages for efficient photocatalytic H₂ generation, *Adv. Mater. Interfaces* 31 (41) (2019) 1903404.

[26] W.-H. Yuan, X.-C. Liu, L. Li, Improving photocatalytic performance for hydrogen generation over Co-doped ZnIn₂S₄ under visible light, *Acta Phys. -Chim. Sin.* 29 (1) (2013) 151–156.

[27] X. Shi, L. Mao, C. Dai, et al., Inert basal plane activation of two-dimensional ZnIn₂S₄ via Ni atom doping for enhanced co-catalyst free photocatalytic hydrogen evolution, *J. Mater. Chem. A* 8 (26) (2020) 13376–13384.

[28] F. Xing, C. Cheng, J. Zhang, et al., Tunable charge transfer efficiency in H_xMoO₃@ZnIn₂S₄ hierarchical direct Z-scheme heterojunction toward efficient visible-light-driven hydrogen evolution, *Appl. Catal. B: Environ.* 285 (2021), 119818.

[29] L. Li, D. Ma, Q. Xu, et al., Constructing hierarchical ZnIn₂S₄/g-C₃N₄ S-scheme heterojunction for boosted CO₂ photoreduction performance, *Chem. Eng. J.* 437 (2022), 135153.

[30] B. Qiu, P. Huang, C. Lian, et al., Realization of all-in-one hydrogen-evolving photocatalysts via selective atomic substitution, *Appl. Catal. B: Environ.* 298 (2021), 120518.

[31] S. Zhang, Z. Zhang, Y. Si, et al., Gradient hydrogen migration modulated with self-adapting S vacancy in copper-doped ZnIn₂S₄ nanosheet for photocatalytic hydrogen evolution, *ACS Nano* 15 (9) (2021) 15238–15248.

[32] W. Wang, M.O. Tadé, Z. Shao, Nitrogen-doped simple and complex oxides for photocatalysis: a review, *Prog. Mater. Sci.* 92 (2018) 33–63.

[33] Y. Pan, X. Yuan, L. Jiang, et al., Recent advances in synthesis, modification and photocatalytic applications of micro/nano-structured zinc indium sulfide, *Chem. Eng. J.* 354 (2018) 407–431.

[34] S. Zhang, M. Du, Z. Xing, et al., Defect-rich and electron-rich mesoporous Ti-MOFs based NH₂-MIL-125 (Ti)@ZnIn₂S₄/CdS hierarchical tandem heterojunctions with improved charge separation and enhanced solar-driven photocatalytic performance, *Appl. Catal. B: Environ.* 262 (2020), 118202.

[35] Y. Qin, H. Li, J. Lu, et al., Synergy between van der waals heterojunction and vacancy in ZnIn₂S₄/g-C₃N₄ 2D/2D photocatalysts for enhanced photocatalytic hydrogen evolution, *Appl. Catal. B: Environ.* 277 (2020), 119254.

[36] G. Zuo, Y. Wang, W.L. Teo, et al., Direct Z-scheme TiO₂–ZnIn₂S₄ nanoflowers for cocatalyst-free photocatalytic water splitting, *Appl. Catal. B: Environ.* 291 (2021), 120126.

[37] W.-K. Chong, B.-J. Ng, C.-C. Er, et al., Insights from density functional theory calculations on heteroatom P-doped ZnIn₂S₄ bilayer nanosheets with atomic-level charge steering for photocatalytic water splitting, *Sci. Rep.* 12 (1) (2022) 1–11.

[38] C. Han, Y.H. Li, J.Y. Li, et al., Cooperative syngas production and C–N bond formation in one photoredox cycle, *Angew. Chem.* 133 (14) (2021) 8041–8049.

[39] Q. Feng, H. Liu, M. Zhu, et al., Electrostatic functionalization and passivation of water-exfoliated few-layer black phosphorus by poly dimethyldiallyl ammonium chloride and its ultrafast laser application, *ACS Appl. Mater. Interfaces* 10 (11) (2018) 9679–9687.

[40] L. Pauling, M. Simonetta, Bond orbitals and bond energy in elementary phosphorus, *J. Chem. Phys.* 20 (1) (1952) 29–34.

[41] W. Liu, S. Ju, X. Yu, Phosphorus-amine-based synthesis of nanoscale red phosphorus for application to sodium-ion batteries, *ACS Nano* 14 (1) (2019) 974–984.

[42] S. Zhang, X. Liu, C. Liu, et al., MoS₂ quantum dot growth induced by S vacancies in a ZnIn₂S₄ monolayer: atomic-level heterostructure for photocatalytic hydrogen production, *ACS Nano* 12 (1) (2018) 751–758.

[43] B. Lin, G. Yang, L. Wang, Stacking-layer-number dependence of water adsorption in 3D ordered close-packed g-C₃N₄ nanosphere arrays for photocatalytic hydrogen evolution, *Angew. Chem.* 131 (14) (2019) 4635–4639.

[44] R. Shi, H.F. Ye, F. Liang, et al., Interstitial P-doped CdS with long-lived photogenerated electrons for photocatalytic water splitting without sacrificial agents, *Adv. Mater.* 30 (6) (2018) 1705941.

[45] Z. Mei, G. Wang, S. Yan, et al., Rapid microwave-assisted synthesis of 2D/1D ZnIn₂S₄/TiO₂ S-scheme heterojunction for catalyzing photocatalytic hydrogen evolution, *Acta Phys. -Chim. Sin.* 37 (6) (2021) 2009097.

[46] E. Zhang, Q. Zhu, J. Huang, et al., Visually resolving the direct Z-scheme heterojunction in CdS@ZnIn₂S₄ hollow cubes for photocatalytic evolution of H₂ and H₂O₂ from pure water, *Appl. Catal. B: Environ.* 293 (2021), 120213.

[47] X. Chen, C. Burda, The electronic origin of the visible-light absorption properties of C-, N- and S-doped TiO₂ nanomaterials, *J. Am. Chem. Soc.* 130 (15) (2008) 5018–5019.

[48] P. Zhou, Q. Zhang, Z. Xu, et al., Atomically dispersed Co-P₃ on CdS nanorods with electron-rich feature boosts photocatalysis, *Adv. Mater.* 32 (7) (2020) 1904249.

[49] X. Jiao, Z. Chen, X. Li, et al., Defect-mediated electron–hole separation in one-unit-cell ZnIn₂S₄ layers for boosted solar-driven CO₂ reduction, *J. Am. Chem. Soc.* 139 (22) (2017) 7586–7594.

[50] H. Li, W. Ali, Z. Wang, et al., Enhancing hot-electron generation and transfer from metal to semiconductor in a plasmonic absorber, *Nano Energy* 63 (2019), 103873.

[51] M.K. Bhunia, S. Melissen, M.R. Parida, et al., Dendritic tip-on polytriazine-based carbon nitride photocatalyst with high hydrogen evolution activity, *Chem. Mater.* 27 (24) (2015) 8237–8247.

[52] M. Wang, C.L. Dong, Y.C. Huang, et al., Electronic structure evolution in tricomponent metal phosphides with reduced activation energy for efficient electrocatalytic oxygen evolution, *Small* 14 (35) (2018) 1801756.

[53] X.-L. Yin, L.-L. Li, Y. Lu, et al., Pomegranate-like Zn_xCd_{1-x}S@MoS₂ nano-heterostructure as a stable and efficient photocatalyst for H₂ evolution, *Mater. Sci. Semicond. Process* 138 (2022), 106287.

[54] X. Zong, H. Yan, G. Wu, et al., Enhancement of photocatalytic H₂ evolution on CdS by loading MoS₂ as cocatalyst under visible light irradiation, *J. Am. Chem. Soc.* 130 (23) (2008) 7176–7177.

[55] Y. Yu, G. Chen, Q. Wang, et al., Hierarchical architectures of porous ZnS-based microspheres by assembly of heterostructure nanoflakes: lateral oriented attachment mechanism and enhanced photocatalytic activity, *Energy Environ. Sci.* 4 (9) (2011) 3652–3660.

[56] M.Z. Rahman, C.W. Kwong, K. Davey, et al., Correction: 2D phosphorene as a water splitting photocatalyst: fundamentals to applications, *Energy Environ. Sci.* 9 (4) (2016) 1513–1514.

[57] X. Wang, L. Bai, J. Lu, et al., Rapid activation of platinum with black phosphorus for efficient hydrogen evolution, *Angew. Chem.* 131 (52) (2019) 19236–19242.